A 2D Kinematic Study of the NLR of the Galaxy NGC 4151

Ramiro D. Simões Lopes
Instituto de Física - Universidade Federal do Rio Grande do Sul

ramirosl@if.ufrgs.br

November 12, 2007

Received _____; accepted _____

Contents

List of Figures

1. Introduction

NGC 4151 is one the six original galaxies with broad high-excitation nuclear emission lines detected by Seyfert (1943). Galaxies with these characteristics became known as Seyfert galaxies - later found to be part of a larger group of galaxies which exhibit unusual phenomena in their nuclei that cannot be attributed to stars (Peterson 1997). These galaxies are called active galaxies or said to host an active galactic nucleus (AGN).

1.1. Active Galactic Nucleus

Today it is known that approximately 43% of all galaxies are active to some degree (Ho et al. 1997). The main classes of AGNs are Quasars, Seyfert galaxies, and Low-Ionization Nuclear Emission Region galaxies (LINERs), the most common ones in the near Universe. Seyferts and LINERs can in addition be classified as type 1 when broad emission lines are present or type 2 when these lines cannot be detected.

In order to explain all AGN types an Unified Model (Antonucci 1993) was proposed which consists of a central supermassive black hole surrounded by a hot accretion disk. As the infalling material spirals into the black hole it is heated to high temperatures giving rise to emission in all wavelengths. Close to the accretion disk, gas clouds moving at high orbital velocities produce broad emission lines. This region, unresolved with present technology, is called the Broad Line Region (BLR). The BLR is shrouded by a thick molecular torus which depending on the viewing angle can block our view of the nucleus. When this happens broad emission lines are not detected and the AGN is of type 2. Otherwise, when the opening of the torus lies in our line of sight the BLR can be seen and the AGN is classified as type 1. There are also narrow emission lines which arise at gas clouds orbiting the nucleus farther away and which are illuminated by the AGN. This region is known as the Narrow Line Region (NLR).

Present studies suggest that only a small fraction of the infalling material is accreted onto the black hole - most is ejected from the nucleus by thermal or magnetocentifugal winds or by powerful radio-plasma jets both of which are detected in the majority of the active galaxies (Crenshaw et al. 2003; Vilkoviskij et al. 2006). These outflows from the nucleus can be understood as a feedback mechanism from the AGN - inflow must happen

to trigger and fuel the activity and as a response matter and radiation are ejected from the nucleus and interact with the galaxy ISM. The amount of energy deposited by these outflows of gas and radiation can be large enough to influence the large scale galactic structure bearing important consequences to galaxy formation and evolution.

1.2. The Narrow Line Region

The NLR is an excellent probe of AGN physics as it is small enough to be under the influence of the AGN - e.g. - to be ionized by the AGN and be pushed by nuclear jets and outflows from the accretion disk, but large enough to be resolved for the nearest galaxies. These processes are predominantly powered by the central engine thus understanding the inflow and outflow physics at this small scales is understanding the physics behind nuclear activity.

At large scales, inflow is more or less accepted to happen as a consequence of interactions of galaxies and perturbations due to non axis-symmetric structures such as large scale bars and spiral arms. At small scales however, inflow mechanisms are still poorly understood. But the first firm clues were provided by Fathi et al. (2006); Storchi-Bergmann et al. (2007) as these authors measured for the first time streaming motions of gas towards the nucleus along nuclear spiral arms traced by dust obscuration and Simões Lopes et al. (2007) found that dust structures, either irregular or in the form of nuclear spirals are ubiquitous in early-type active galaxies.

Similarly to the case of inflow, outflow mechanisms are yet to be fully understood. Nevertheless outflows of gas have reportedly been detected in the NLR of active galaxies mostly in the form of ionized bicones. Gas in these bicones is probably accelerated by thermal expansion, radiation pressure, magnetic fields or a combination of these processes (Proga 2007) while the ionization is either provided by photoionization by the AGN, shocks with the radio jet or both.

1.3. The Galaxy NGC 4151

The galaxy NGC 4151 is a nearby Seyfert 1.5 with a recession velocity of $\sim 997\ \mathrm{km\,s^{-1}}$ (Pedlar et al. 1992) which corresponds to a distance of approximately ~ 13.3 Mpc and a

linear spatial scale of $\sim$ 64 pc arcsec^{-1} assuming H_0 = 75 km s^{-1} . It is a grand-design weakly barred spiral galaxy seen almost face-on, i $\sim$ 21°, and the galaxy major axis (MA) is at a position angle (PA) of 22° measured counter-clockwise from the N. The NLR of NGC 4151 is very rich with several distinct kinematic components at different position angles which should presumably make it easier to distinguish the influence of each one on the dynamics of the NLR. The geometry of the NLR is largely dominated by an ionization cone traced in the optical by [O III] emission at PA 60° with associated outflows detected in absorption at UV and X-rays, and which was modeled as a biconical outflow of gas by Das et al. (2005); Crenshaw et al. (2000); Hutchings et al. (1999). These authors also pointed out that the AGN should be the primary ionization source of the bicone as no apparent correlation with the radio jet, seen at PA $\sim$ 77° (Mundell et al. 2003), could be established. The presence of a weak fat bar at PA 130° was confirmed by Mundell and Shone (1999) who also detected H I inflow produced at the shock fronts of the bar indicating a possible feeding channel to the AGN at kpc scales. Despite being a very well studied galaxy, see Ulrich (2000) the dynamics and excitation of the NLR, as well as the role of the radio jet, are yet not fully understood. New, unprecedent IFU data can bring new information about the NLR and help to clear out our understanding of AGN physics.

2. Objectives

Our goal is to produce 2D kinematics and flux maps of the NLR of the galaxy NGC 4151 and to create a phenomenological model for the observed outflow in order to better understand the NGC 4151 NLR and AGN physics.

3. The Data

The galaxy NGC 4151 was observed at the Z, J, H and K bands at three field locations with the Near Infrared Integral Field Spectrograph (NIFS) (McGregor et al. 2003) instrument of the Gemini North Telescope. After mosaicing the observations cover a contiguous field of 3 x 8 arcsec^2 and a spectral region from 0.95 to 2.40 μm. The observations and data reduction were carried out by our collaborators as part of the NIFS science verification program. Figure 1 shows an image of the galaxy obtained with the

Jacobus Kapteyn Telescope (JKT) and our NIFS field superposed on the HST/FOC [O III] image of Winge et al. (1997), and figure 2 shows the galaxy spectrum at the nucleus (upper) and at a region distant 1 arcsec from the nucleus (lower).

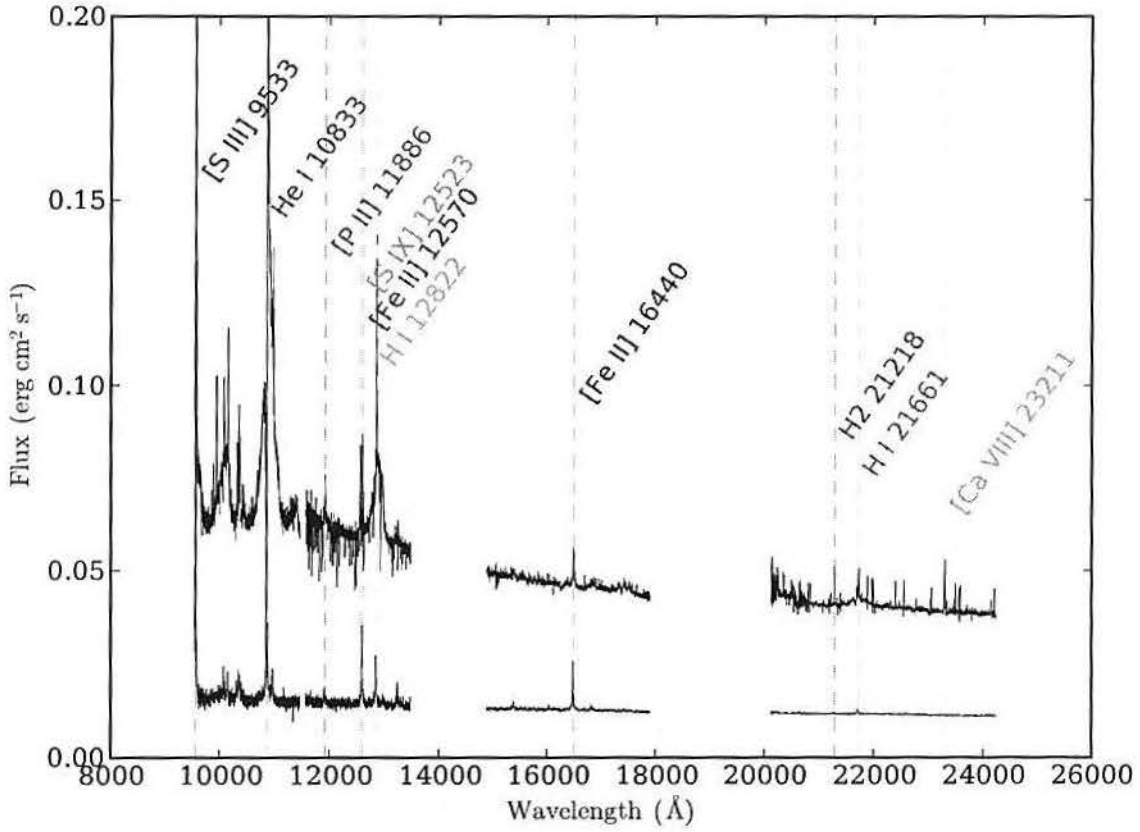

Fig. 2.— Z, J, H, and K band spectra of the galaxy NGC 4151 taken at the nucleus (upper) and at a point distant 1 arcsec from the nucleus (lower).

NIFS is an Integral Field Unity (IFU) with a 2048 x 2048 pixels CCD corresponding to a field of 3 x 3 arcsec^2 in the sky. The use of adaptive optics allows NIFS to achieve resolutions of up to 0.1 arcsec and the spectral resolving power R $\sim$ 5300 gives an uncertainty of $\sim$ 3 Å in wavelength, equivalent to $\sim$ 56 km s^{-1} in velocity space. IFUs have the unique capability of acquiring independent spectra for each pixel on the CCD. The two-dimensional (2D) coverage provides detailed kinematic mappings that cannot be obtained with long slit spectroscopy. After all reduction steps are performed a data cube is

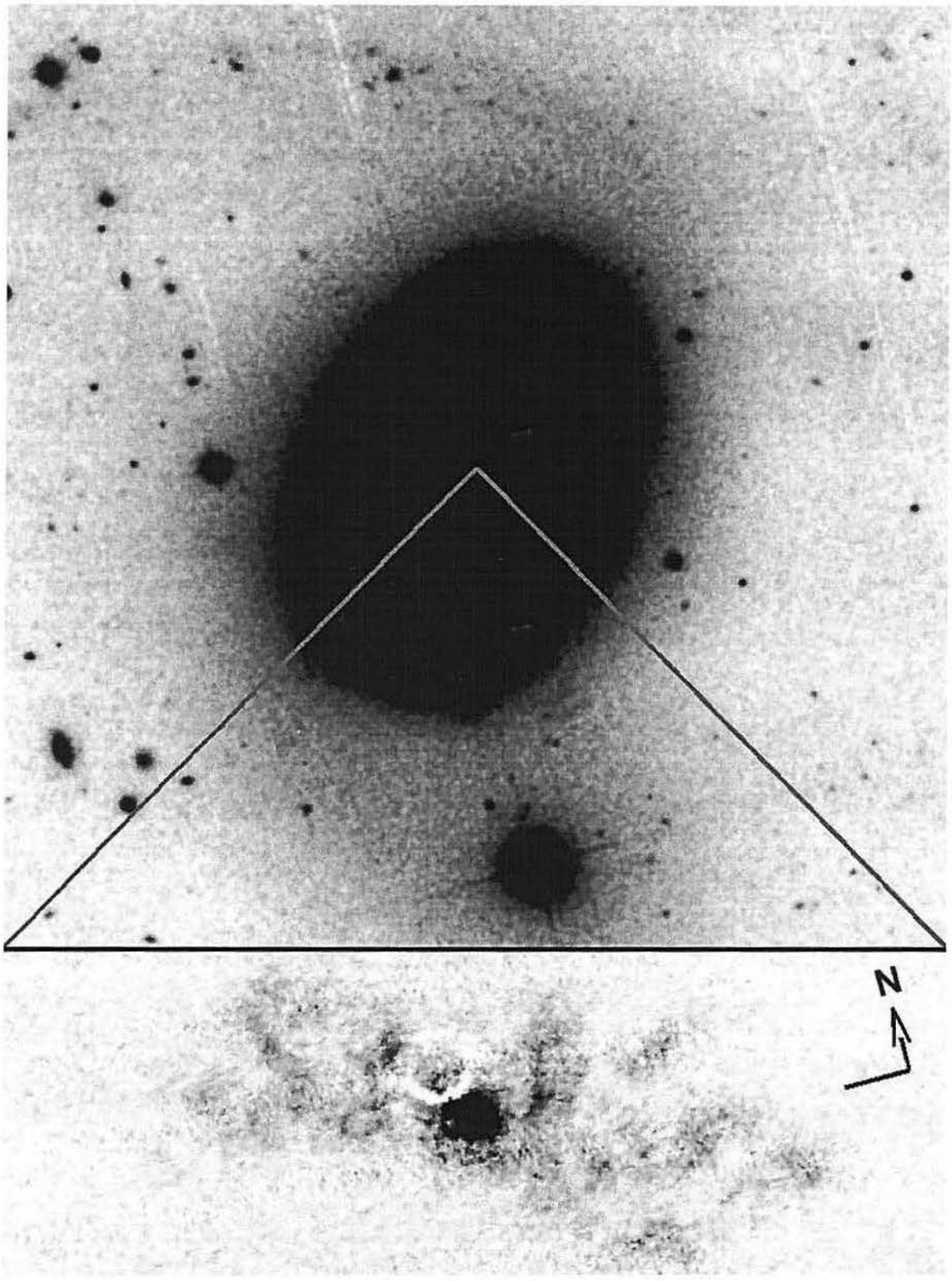

Fig. 1.— Upper panel: JKT image of the galaxy NGC 4151 with the observed field unresolved on the center, the whole image covers 6.8 x 6.8 arcmin^2 of the sky. Lower panel: NIFS observations field-of-view covering 3 x 8 arcsec^2 of the sky, showing the HST/FOC continuum subtracted optical [O III] image (Winge et al. 1997).

generated with two spatial directions and one spectral direction.

Our data consists of 4 data cubes, one for each (Z, J, H and K) band, with 78 x 70 spatial pixels yielding a total of 5460 spectra per band.

4. Analysis

The analysis consists of the measurement of the integrated fluxes, Doppler shifts and broadening of the emission lines from the NLR through the fit of Gaussians to the emission lines.

Due to the large number of spectra generated by the observations, the analysis of IFU data requires the use of automated methods. For this task we developed an algorithm to optimize the fitting of Gaussian profiles to the emission lines done by *IRAF*[1] software package. The procedures to construct flux, radial velocity and velocity dispersion (σ) maps are detailed below:

4.1. Emission Line Fluxes

Emission line flux maps are produced by integrating the total flux under each emission line, what corresponds to slice the data cube over a spectral interval centered on the emission line wavelength in the galaxy rest frame and subtract a continuum level produced by averaging the fluxes of spectral regions at each side of the emission line.

4.2. Radial Velocity and Velocity Dispersion

Through the fit of Gaussian profiles it is possible to measure the gas radial velocity and velocity dispersion. The difference in wavelength between the center of the fitted Gaussian profile and the rest frame wavelength of the emission line is a measure of the Doppler shift

[1] *IRAF* is the Image Reduction and Analysis Facility, a general purpose software system for the reduction and analysis of astronomical data. Fitprofs is a task which performs profile fitting the spectral lines. *IRAF* is written and supported by the *IRAF* programing group at the National Optical Astronomy Laboratories (NOAO).

produced by the relative velocity between the Earth and the observed gas. Gas velocities can then be calculated with the formula:

$$v = \frac{\Delta\lambda}{\lambda}c - v_s$$

Where $v_s = 997\ \mathrm{km\,s^{-1}}$ is the adopted galaxy systemic velocity.

Emission lines arising in gas clouds moving away from us will be redshifted to longer wavelengths while emission lines from gas clouds moving towards us will be blueshifted to shorter wavelengths.

Gas clouds moving with a slightly different velocity than the average will produce a broadening of the emission line profile in such a way that the gas velocity dispersion is related with the Full Width at Half Maximum (FWHM) of the fitted Gaussian and can be calculated through the formula $\sigma = FWHM/2.35$.

4.3. Profile Fitting

The *IRAF fitprofs* task was used to fit the IFU 2D spectra. Nevertheless *fitprofs* requires and relies on only one initial guess for the central wavelength. This limitation poses a problem to IFU data analysis as the central wavelengths of the emission lines vary a lot along the field resulting in poor fits to most of the data. In order to surpass this limitation and optimize the fitting we developed an algorithm that allows the input of multiple guesses to the fitting routine. The algorithm works as follows: first it reads a table with initial guess values to the central wavelengths (previously measured) of emission lines at several points over the observed field; then, in order to increase the number of guesses it triangulates the points and adds new guesses at the centers of the triangles whose values are the arithmetic mean of the three corresponding vertices. It then proceeds to the fitting with *fitprofs* using as initial value for each point the closest guess available. This way the fitting is enhanced and optimized for the whole field as can be seen in Fig. 3, the left panel shows the Brγ velocity map produced by *fitprofs* only and the right panel with our *script*. For weak, low signal emission lines the use of our algorithm is essential to extract the maximum information from the data.

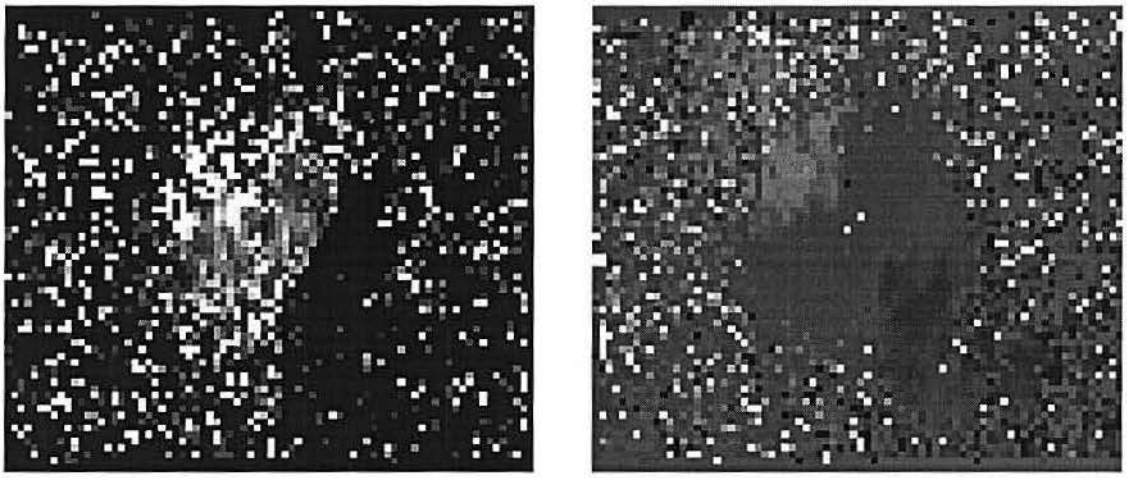

Fig. 3.— Radial velocity maps of the Brγ emission line produced by *fitprofs* (left) and our *script* (right).

In some regions the emission line profiles show double-peaks or wings indicating the existence of more than one component. In most cases however, our spectral resolving power and S/N ratio is not enough to resolve each component making it difficult to distinguish between two or one sole component what turns the fitting routine even more complicated. Thus we fitted two Gaussian profiles only for the strongest lines, [S III] and He I in regions where double-peaks can be clearly seen. Our *script* was also used to perform multi-component fits as follows: First it proceeds to a single component fit as described above; then it uses the results of the fit as guesses to a new fit with two Gaussian profiles. The guesses for the central wavelengths of each Gaussian profile is that found for the single fit $\pm$ the FWHM/2. Figure 4 displays typical single and double-peaked emission line profiles and the Gaussian fits performed by our script and *fitprofs*.

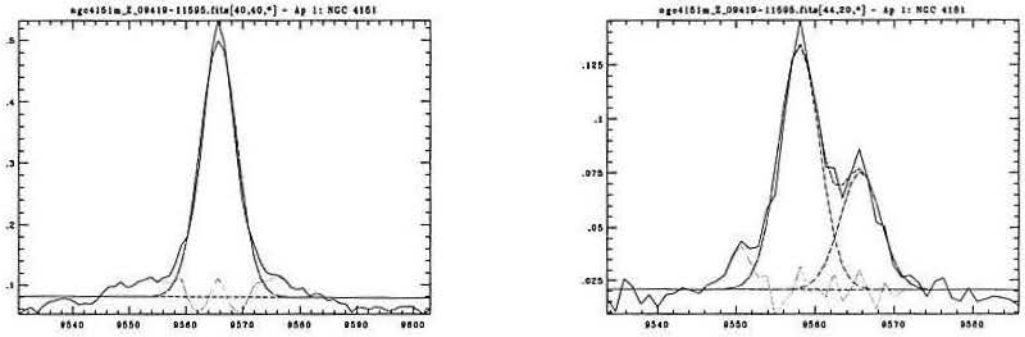

Fig. 4.— Typical single (left) and double-peaked (right) emission line profiles. The dashed line represents the fitted Gaussian profile.

5. Results

We measured the following emission lines in the Z band: [S III] λ9533.2 and He I λ10833.2167; in the J band: [P II] λ11886.10, [S IX] 12523, [Fe II] 1257-.238 and [Pa β] 12821.59; in the H band: [Fe II] 16439.981; and in the K band: H_2 21218.20, [Br γ] 21661.20 and [Ca VIII] 23211. We produced two-dimensional flux, radial velocity and σ maps for each of these lines which are shown in Figs. 5-14. For the [S III] and He I emission lines we show the two component fit and also the single component fit to aid visualization and compare with the other lines.

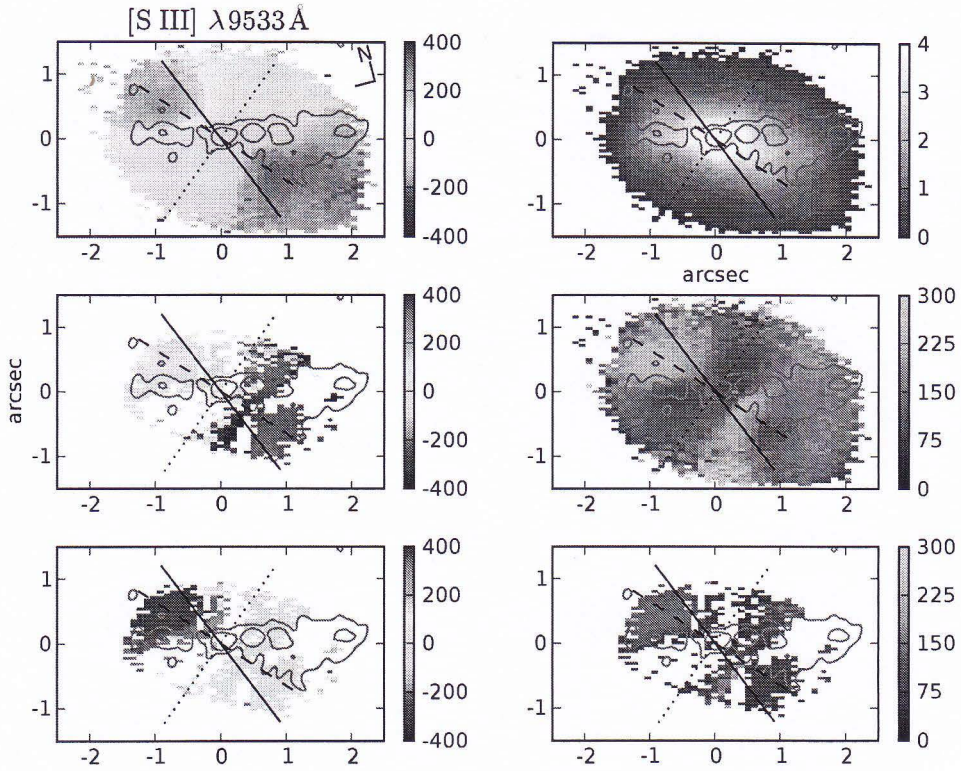

Fig. 5.— Left: [S III] single component fit (top), component B (middle) and component R (bottom) radial velocity maps. Right: Integrated flux (top), single component fit (middle) and two component fit (bottom) σ maps. The continuous, dashed and dotted lines represent the galaxy MA, bicone axis, and the bar respectively. Contours show the λ 21 cm MERLIN image.

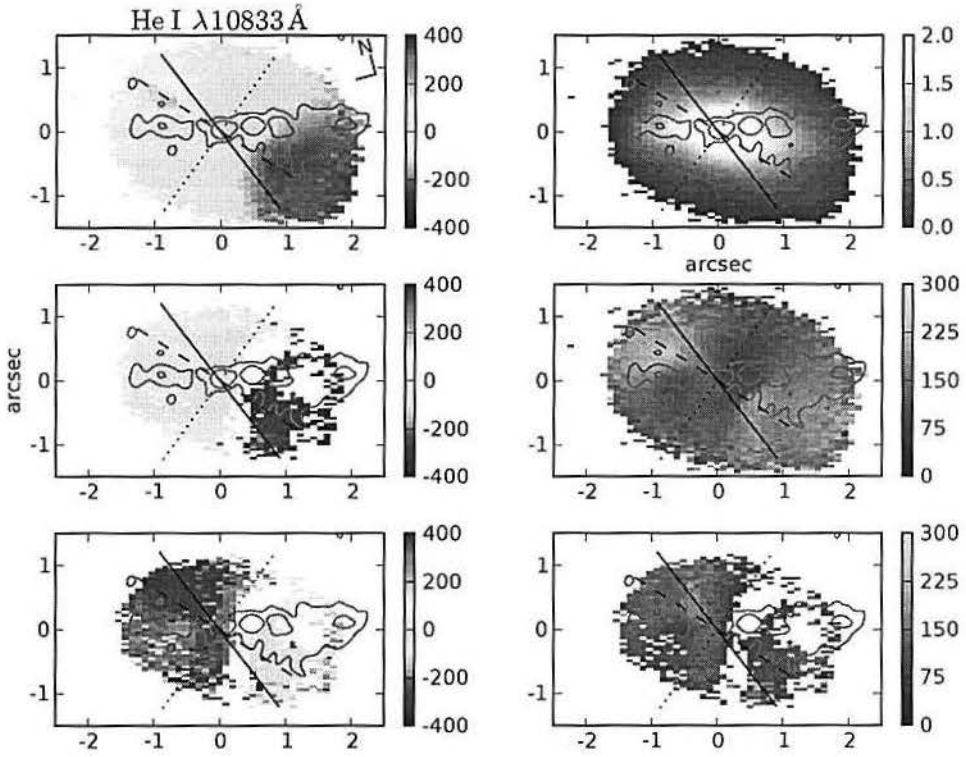

Fig. 6.— Left: He I single component fit (top), component B (middle) and component R (bottom) radial velocity maps. Right: Integrated flux (top), single component fit (middle) and two component fit (bottom) σ maps.The continuous, dashed and dotted lines represent the galaxy MA, bicone axis, and the bar respectively. Contours show the λ 21 cm MERLIN image.

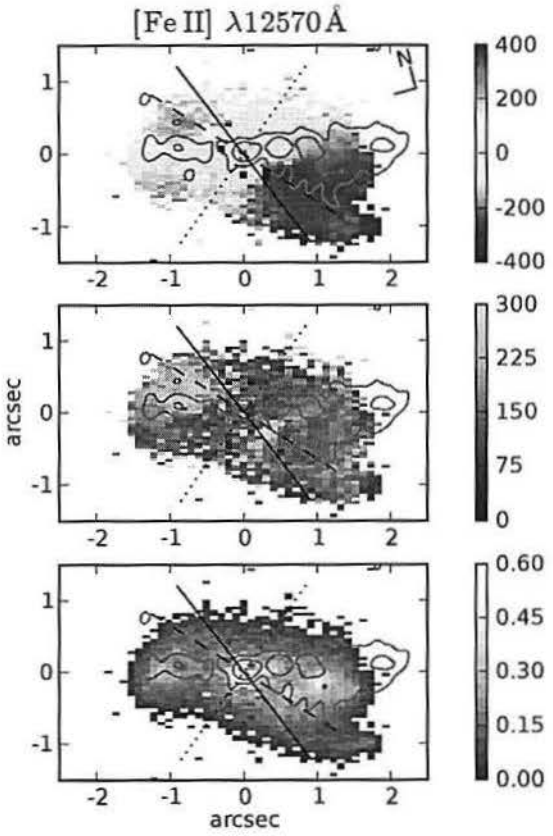

Fig. 7.— [Fe II] radial velocity (top), σ (middle) and flux (bottom) maps. The continuous, dashed and dotted lines represent the galaxy MA, bicone axis, and the bar respectively. Contours show the λ 21 cm MERLIN image.

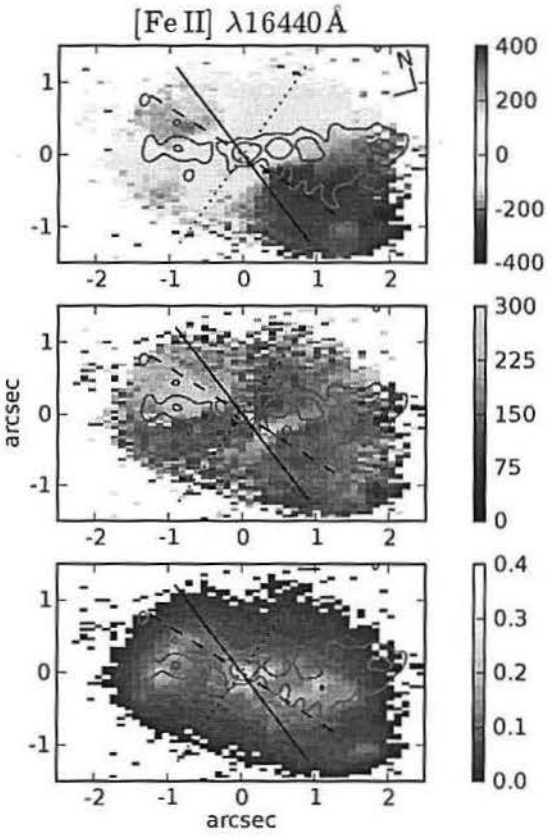

Fig. 8.— [Fe II] radial velocity (top), σ (middle) and flux (bottom) maps. The continuous, dashed and dotted lines represent the galaxy MA, bicone axis, and the bar respectively. Contours show the λ 21 cm MERLIN image.

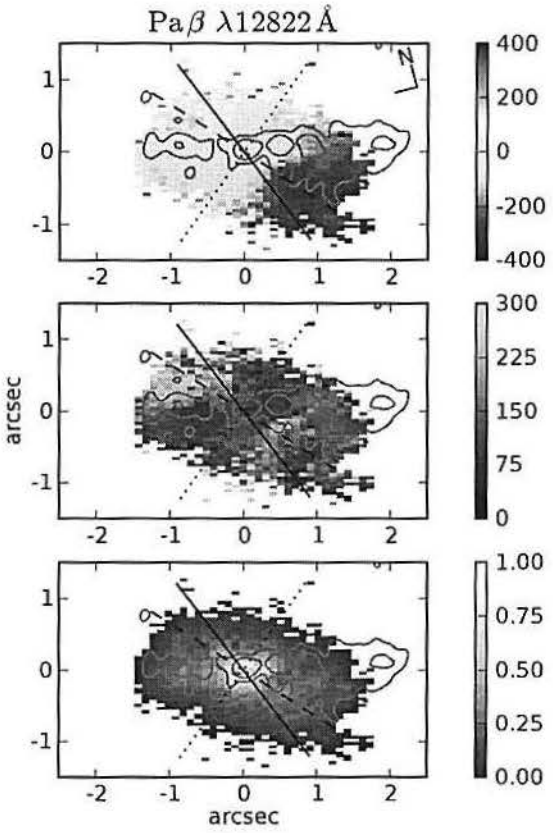

Fig. 9.— Paβ radial velocity (top), σ (middle) and flux (bottom) maps. The continuous, dashed and dotted lines represent the galaxy MA, bicone axis, and the bar respectively. Contours show the λ 21 cm MERLIN image.

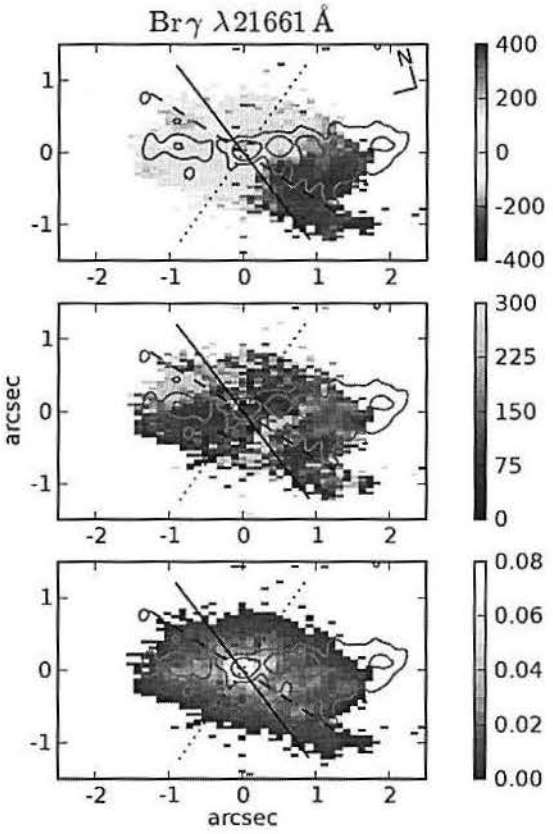

Fig. 10.— Br γ radial velocity (top), σ (middle) and flux (bottom) maps. The continuous, dashed and dotted lines represent the galaxy MA, bicone axis, and the bar respectively. Contours show the λ 21 cm MERLIN image.

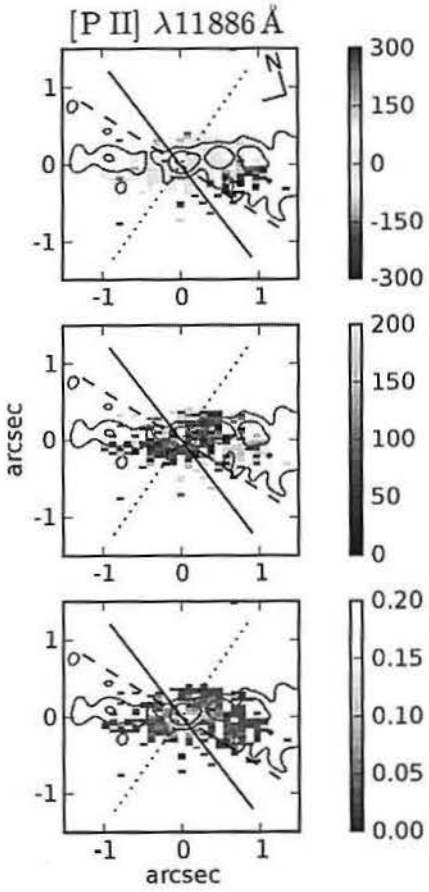

Fig. 11.— [P II] radial velocity (top), σ (middle) and flux (bottom) maps. The continuous, dashed and dotted lines represent the galaxy MA, bicone axis, and the bar respectively. Contours show the λ 21 cm MERLIN image.

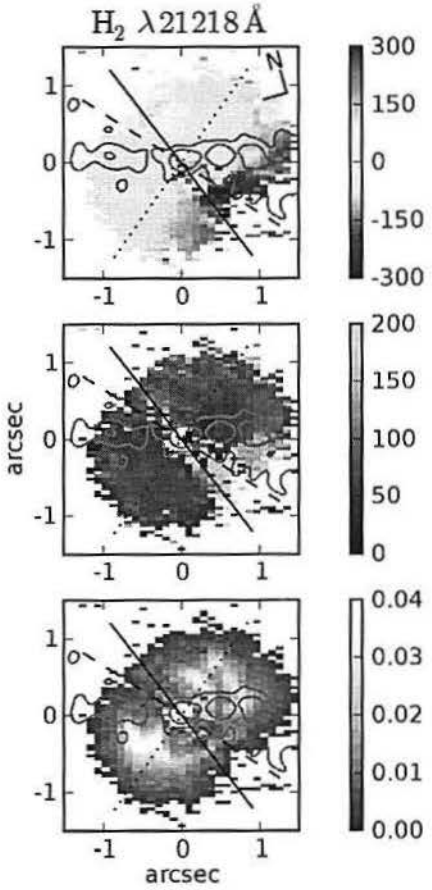

Fig. 12.— H_2 radial velocity (top), σ (middle) and flux (bottom) maps. The continuous, dashed and dotted lines represent the galaxy MA, bicone axis, and the bar respectively. Contours show the λ 21 cm MERLIN image.

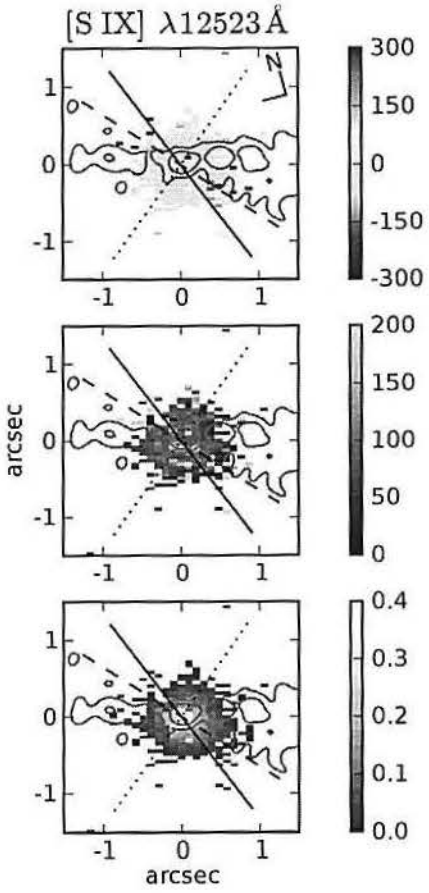

Fig. 13.— [S IX] radial velocity (top), σ (middle) and flux (bottom) maps. The continuous, dashed and dotted lines represent the galaxy MA, bicone axis, and the bar respectively. Contours show the λ 21 cm MERLIN image.

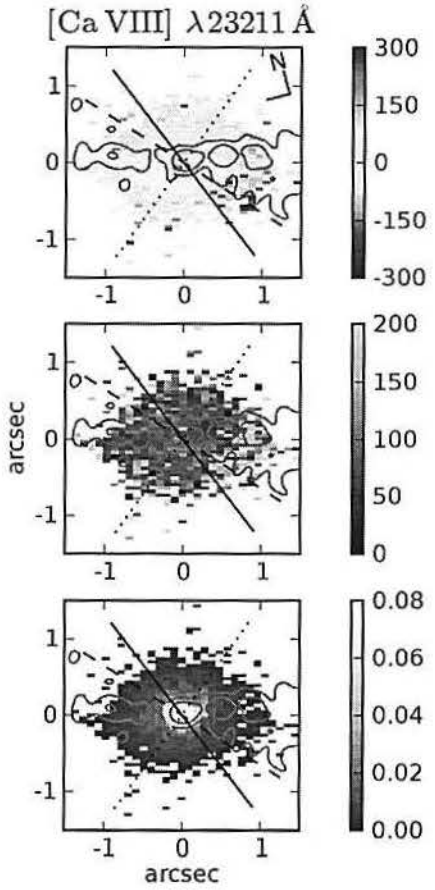

Fig. 14.— [Ca VIII] radial velocity (top), σ (middle) and flux (bottom) maps. The continuous, dashed and dotted lines represent the galaxy MA, bicone axis, and the bar respectively. Contours show the λ21 cm MERLIN image.

5.1. Flux Distributions

The flux distributions in the [S III], He I, [Fe II], H I, and [P II] emission lines (Figs. 5 to 11) are very similar being elongated and following approximately the PA of the bicone axis $\sim 58°$. On the other hand there is a weak trend for these lines to align with the radio axis specially to the NE. To the SW the region with highest flux spreads out to a wider angle relative to the nucleus than to the NE, a characteristic also seen on the radio jet. Also

some knots of emission can be seen, more clearly for the [Fe II] and H I lines which seem to show a relation with the observed radio emission knots. We also measured emission from regions outside the bicone.

The H_2 flux distribution (Fig. 12) on the other hand is oriented at a different PA than the other emission lines, approximately following the orientation of the large scale bar at PA $\sim 130°$ avoiding both the radio and the bicone axis. Regions of high flux with a "banana" shaped morphology resembling shock fronts can be seen at both the NW and SE sides of the nucleus while some points at the center does not show any emission.

The [S IX] and [Ca VIII] emission lines (Figs. 13 and 14) are coronal lines and their flux distribution is more compact, decreasing with increasing radial distance from the center showing no relationship with the bicone, radio jet or the bar.

5.2. Radial Velocity

The kinematics of the single component fit of the [S III], He I, [Fe II], H I, and [P II] emission lines (Figs. 5 to 11) is largely dominated by the biconical outflow with gas velocities increasing radially from the bicone origin until a maximum velocity of $\sim \pm$ 400 km s^{-1} at 1 arcsec from the nucleus (blueshifted at SW and redshifted at NE) where it starts to decrease. Outside the bicone the emission lines are approximately at the galaxy systemic velocity.

The H_2 kinematics (Fig. 12) show some asymmetry with the highest blueshifts of $\sim$ -230 km s^{-1} between the bicone axis and the galaxy MA to the SW but with the highest redshifts of $\sim$ 130 km s^{-1} along the galaxy MA to the NE. Some blueshifts are also seen to the W, along the radio jet and away from the bicone axis at 1.5 arcsec from the center. Similarly to the other emission lines, far from the bicone axis or the galaxy MA the velocities are close to systemic.

The [S IX] and [Ca VIII] velocities (Figs. 13 and 14) are close to systemic throughout the field.

5.3. Velocity Dispersion (σ)

The velocity dispersion maps are similar for the [S III], He I, [Fe II], H I, and [P II] emission lines (Figs. 5 to 11) with three regions of high velocity dispersion: at both ends of the bicone to NE and SW and at an elongated region at PA $\sim 125°$ offset $\sim 0.5''$ from the nucleus to the SW. For the [He I] the highest σs are found at both ends of the bicone and to the SW it seems to merge with the elongated structure seen at the other σ maps. The maximum velocity dispersions are ~ 350 km s^{-1} and the minimum ~ 50 km s^{-1}.

The H_2 σ map (Fig. 12) shows the highest values (~ 250 km s^{-1}) in the regions with the highest velocities and the lowest values (~ 40 km s^{-1}) in the regions with lowest velocities.

The [S IX] and [Ca VIII] σ maps (Figs. 13 and 14) show values of ~ 100 km s^{-1} throughout the field.

5.4. Two Components Fit: [S III] and He I

We were able to resolve and measure the two components of the [S III] and He I emission lines in a region from $\sim$ -1 to 1 arcsec from the nucleus oriented along the bicone axis.

For the two components fit of the [S III] line (Fig. 5) we can see that to the NE both components (B and R) are redshifted while to the SW both are blueshifted. The minimum absolute velocities of each component are close to systemic both to the NE and SW, while the maximum velocity show some asymmetry reaching $\sim$ -200 km s^{-1} to the SW in component R and ~ 500 km s^{-1} to the NE in component B.

For the He I emission line (Fig. 6) two components were present over a larger region than for the [S III] and as for the [S III] the minimum absolute velocities of each component are close to systemic. But large blueshifts of $\sim$ -350 km s^{-1} are seen to the SW in component R and large redshifts of ~ 500 km s^{-1} are seen to the NE in component B.

The velocity dispersions of the two components were assumed to be the same in the fits, but they show a similar trend as the other lines with single components, with high velocity dispersions at the elongated structure near the nucleus and at the NE opening of

the bicone.

6. Outflow Model

We developed a 2D kinematic model based on our radial velocity maps similar to that of Das et al. (2005); Crenshaw et al. (2000), who fitted a biconical outflow model to their long slit spectroscopic observations of [O III] emitting gas. Our model reproduces the radial velocity map of a biconical outflow originated at the nucleus, in which gas is assumed to flow along the bicone surfaces with velocities increasing from zero to a maximum at the turnover radius according to a law: $v = kr$ and later decreasing with $v = v_{max} - k'r$, where r represents the distance to the origin. The modeled radial velocity map is produced by projecting the velocities along the bicone surfaces into the line-of-sight. Figure 15 shows the bicone geometry and Fig. 16 show the 2D velocity maps produced by our model for each face of the bicone which we call components B and R. We found that our data is best reproduced by a bicone with an axis oriented at position angle $PA = 58\,^{\circ}$, half opening angle $\alpha = 30\,^{\circ}$ and inclination to the line of sight $\theta = 38\,^{\circ}$. The turnover radius (r_t) is located at $\sim$ 1.5 arcsec (projected distance at the galaxy of 96 pc) from the nucleus and the maximum velocity at this distance is $v_m \sim 675\,km\,s^{-1}$. Das et al. (2005) found very similar parameters for their model: $PA = 60\,^{\circ}$, $\alpha = 33 \pm 2\,^{\circ}$, $\theta = 45 \pm 5\,^{\circ}$, $r_t = 96 \pm 16\,pc$ and $v_m = 800 \pm 50\,km\,s^{-1}$ what is not surprising as their data covers just a slightly larger region than ours, and suggests that the [O III] optical emission line kinematics is similar to those of the [S III] and He I lines.

Due to the bicone large opening angle and its inclination to the line-of-sight, component B has the highest blueshifts of $\sim$ -600 km s^{-1} close to the nucleus at $\sim$ 0.3 arcsec SW and the highest redshifts of $\sim$ 400 km s^{-1} at a distance of $\sim 1''$ to NE of the nucleus. Component R is symmetrical to B showing the highest redshifts of $\sim$ 600 km s^{-1} at $\sim$ 0.3 arcsec NE of the nucleus and the highest blueshifts of $\sim$ -400 km s^{-1} at a distance of $\sim 1''$ to the SW of the nucleus.

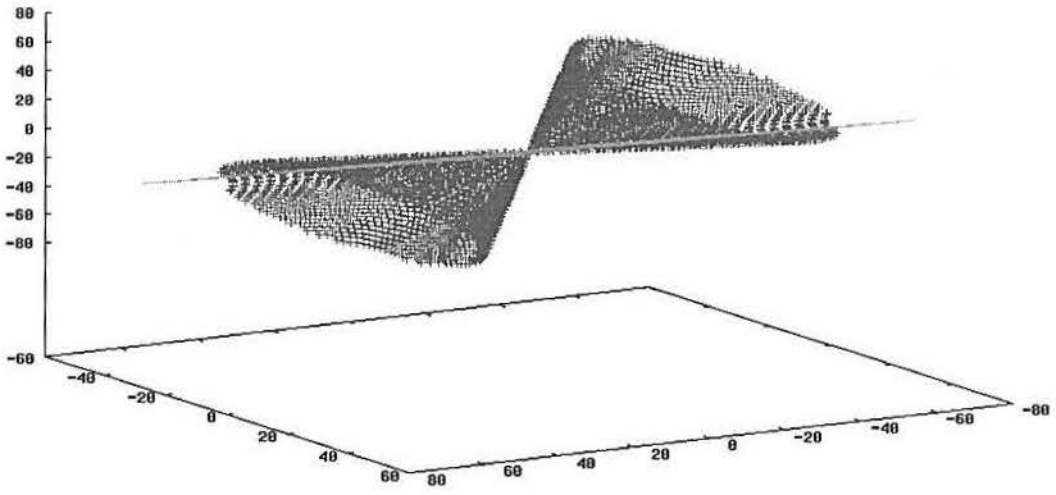

Fig. 15.— Geometry of the bicone model with the green line representing the plane of the galaxy. The line-of-sight is looking down, approximately parallel to the z axis.

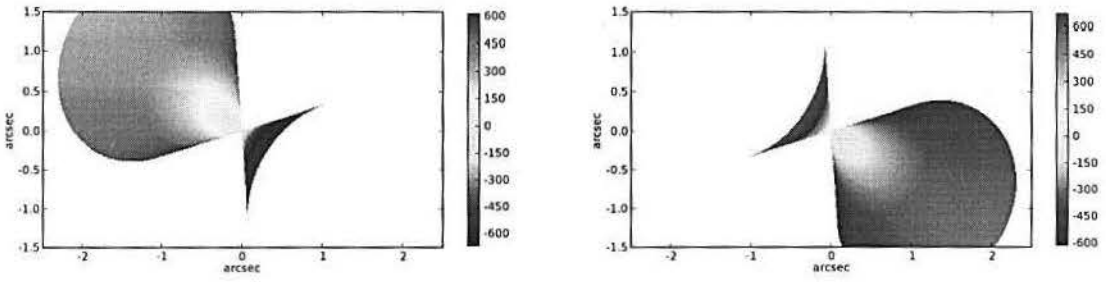

Fig. 16.— Modelled radial velocity maps for component B (left panel) and component A (right panel).

7. Discussion

7.1. The Bicone

The flux distribution and kinematics of the [S III], He I, [Fe II], H I, and [P II] largely traces the biconical outflow. Nevertheless the presence of some high flux clouds and their approximate alignment with the radio knots to the NE suggests a weak correlation with the radio jet. We interpret that these high flux clouds could be formed by compression of the ISM gas by the radio jet, creating regions of higher gas density.

Two emission components were detected for the [S III] and He I emission lines in the region occupied by the bicone. In view of the galaxy inclination angle and PA, and the biconical geometry derived from our model, a portion of the galaxy plane will intersect the bicone to the SW and NE as shown in Fig. 15. Thus, as one of the components measured always shows velocities close to systemic we assume that this component is emitted by gas in the plane and the other by the bicone.

The small increase in σ seen at both endings of the bicone at approximately 1″ from the nucleus could be due to the collision of the outflowing gas with a possible denser ISM at this distance which would also explain the deceleration trend also starting at this distance.

The general trend in the two component fit to the [S III] line is that the bluemost component shows more flux than the redmost component what would be expected if some obscuration is present, considering that the far side of the bicone is partially hidden behind the plane of the galaxy, according to our model. This obscuration however must not be too strong as we see both components along most of the bicone.

7.2. H_2 and the Bar

Interestingly H_2 emission is found to be distributed along the inner ends of the galaxy bar avoiding the bicone region and the radio jet. This can be understood as due to the fact that along the bicone radiation from the AGN probably dissociates most of the H_2 molecules present. The region outside the bicone however must be shielded from the ionizing radiation. The geometry is consistent with the shielding being provided by the dusty torus whose axis would be parallel to the bicone axis . Moreover Mundell and Shone

(1999) detected an inflow of H I along the galaxy bar at large scales. This gas could be the source for the formation of the observed H_2.

The kinematics is dominated by velocities close to systemic, with some redshifts observed to the NE along the galaxy MA and towards the N, while some blueshifts are observed to the SW along the bicone axis and towards the W. This geometry cannot be explained solely by rotation or outflow. Thus it is probable that we are seeing a combination of both movements with the outflowing gas disturbing the rotation pattern and increasing the radial velocities to values higher than the ones that would be produced by rotation only.

7.3. The Radio Jet

The debate over the importance of the radio jet in shaping the NLR of active galaxies is not yet settled and both photoionization (Binette et al. 1996) and shock ionization caused by the passage of the jet (Storchi-Bergmann et al. 2007) are likely sources of ionization. Our data for the galaxy NGC 4151 supports that photoionization is the dominant excitation mechanism in the NLR as no clear correspondence between the radio jet and the NLR structure can be seen. This result is in agreement with the findings of Das et al. (2005); Mundell et al. (2003) whose kinematic analysis revealed that radiation is the most likely source of ionization, and Nelson et al. (2000); Hutchings et al. (1998) who measured emission line ratios which also favored photoionization by the AGN radiation.

8. Conclusions

The NLR of the galaxy NGC 4151 shows a rather complex geometry. The flux distributions and kinematics show that while the biconical outflow is the dominant component, the large scale bar, and to a minor extent, the radio jet also have a role in shaping the NLR.

- The [S III], He I, [Fe II], H I, and [P II] kinematics is largely determined and well modelled by a biconical outflow.
- The bicone parameters derived by our model are: $PA = 58°$, half opening angle $\alpha = 30°$, inclination to the line of sight $\theta = 38°$, turnover radius $r_t \sim 1.5$ arcsec, and

the maximum velocity at this distance $v_m \sim 675\, km\, s^{-1}$.

- The H_2 is distributed along the inner region of the large scale galaxy bar probably tracing the inflow of gas.
- The AGN radiation is the most probable source of ionization of the NLR.
- The radio jet plays a minor role in shaping the NLR of the galaxy NGC 4151.

REFERENCES

Antonucci, R. (1993). Unified models for active galactic nuclei and quasars. *ARA&A*, 31:473–521.

Binette, L., Wilson, A. S., and Storchi-Bergmann, T. (1996). Excitation and temperature of extended gas in active galaxies. II. Photoionization models with matter-bounded clouds. *A&A*, 312:365–379.

Crenshaw, D. M., Kraemer, S. B., and George, I. M. (2003). Mass Loss from the Nuclei of Active Galaxies. *ARA&A*, 41:117–167.

Crenshaw, D. M., Kraemer, S. B., Hutchings, J. B., Bradley, II, L. D., Gull, T. R., Kaiser, M. E., Nelson, C. H., Ruiz, J. R., and Weistrop, D. (2000). A Kinematic Model for the Narrow-Line Region in NGC 4151. *AJ*, 120:1731–1738.

Das, V., Crenshaw, D. M., Hutchings, J. B., Deo, R. P., Kraemer, S. B., Gull, T. R., Kaiser, M. E., Nelson, C. H., and Weistrop, D. (2005). Mapping the Kinematics of the Narrow-Line Region in the Seyfert Galaxy NGC 4151. *AJ*, 130:945–956.

Fathi, K., Storchi-Bergmann, T., Riffel, R. A., Winge, C., Axon, D. J., Robinson, A., Capetti, A., and Marconi, A. (2006). Streaming Motions toward the Supermassive Black Hole in NGC 1097. *ApJ*, 641:L25–L28.

Ho, L. C., Filippenko, A. V., and Sargent, W. L. W. (1997). A Search for "Dwarf" Seyfert Nuclei. V. Demographics of Nuclear Activity in Nearby Galaxies. *ApJ*, 487:568–+.

Hutchings, J. B., Crenshaw, D. M., Danks, A. C., Gull, T. R., Kraemer, S. B., Nelson, C. H., Weistrop, D., Kaiser, M. E., and Joseph, C. L. (1999). High-Velocity Line Emission in the Narrow-Line Region of NGC 4151. *AJ*, 118:2101–2107.

Hutchings, J. B., Crenshaw, D. M., Kaiser, M. E., Kraemer, S. B., Weistrop, D., Baum, S., Bowers, C. W., Feinberg, L. D., Green, R. F., Gull, T. R., Hartig, G. F., Hill, G., and Lindler, D. J. (1998). Gas Cloud Kinematics near the Nucleus of NGC 4151. *ApJ*, 492:L115+.

McGregor, P. J., Hart, J., Conroy, P. G., Pfitzner, M. L., Bloxham, G. J., Jones, D. J., Downing, M. D., Dawson, M., Young, P., Jarnyk, M., and Van Harmelen, J. (2003).

Gemini near-infrared integral field spectrograph (NIFS). In Iye, M. and Moorwood, A. F. M., editors, *Instrument Design and Performance for Optical/Infrared Ground-based Telescopes. Edited by Iye, Masanori; Moorwood, Alan F. M. Proceedings of the SPIE, Volume 4841, pp. 1581-1591 (2003).*, volume 4841 of *Presented at the Society of Photo-Optical Instrumentation Engineers (SPIE) Conference*, pages 1581–1591.

Mundell, C. G. and Shone, D. L. (1999). Gas dynamics in the barred Seyfert galaxy NGC 4151 - I. HI streaming shocks and inflow along the bar. *MNRAS*, 304:475–480.

Mundell, C. G., Wrobel, J. M., Pedlar, A., and Gallimore, J. F. (2003). The Nuclear Regions of the Seyfert Galaxy NGC 4151: Parsec-Scale H I Absorption and a Remarkable Radio Jet. *ApJ*, 583:192–204.

Nelson, C. H., Weistrop, D., Hutchings, J. B., Crenshaw, D. M., Gull, T. R., Kaiser, M. E., Kraemer, S. B., and Lindler, D. (2000). Space Telescope Imaging Spectrograph Long-Slit Spectroscopy of the Narrow-Line Region of NGC 4151. I. Kinematics and Emission-Line Ratios. *ApJ*, 531:257–277.

Pedlar, A., Howley, P., Axon, D. J., and Unger, S. W. (1992). A neutral hydrogen study of NGC 4151. *MNRAS*, 259:369–380.

Peterson, B. M. (1997). *An Introduction to Active Galactic Nuclei.* An introduction to active galactic nuclei, Publisher: Cambridge, New York Cambridge University Press, 1997 Physical description xvi, 238 p. ISBN 0521473489.

Proga, D. (2007). Theory of Winds in AGNs. In Ho, L. C. and Wang, J.-W., editors, *Astronomical Society of the Pacific Conference Series*, volume 373 of *Astronomical Society of the Pacific Conference Series*, pages 267–+.

Seyfert, C. K. (1943). Nuclear emission in spiral nebulae. *ApJ*, 97:28–+.

Simões Lopes, R. D., Storchi-Bergmann, T., de Fátima Saraiva, M., and Martini, P. (2007). A Strong Correlation between Circumnuclear Dust and Black Hole Accretion in Early-Type Galaxies. *ApJ*, 655:718–734.

Storchi-Bergmann, T., Dors, Jr., O. L., Riffel, R. A., Fathi, K., Axon, D. J., Robinson, A., Marconi, A., and Ostlin, G. (2007). Nuclear spirals as feeding channels to the Supermassive Black Hole: the case of the galaxy NGC 6951. *ArXiv e-prints*, 707.

Ulrich, M.-H. (2000). The active galaxy NGC 4151: Archetype or exception? *A&A Rev.*, 10:135–178.

Vilkoviskij, E. Y., Lovelace, R. V. E., Pavlova, L. A., Romanova, M. M., and Yefimov, S. N. (2006). Matter Outflows from AGN: A Unifying Model. *Ap&SS*, 306:129–137.

Winge, C., Axon, D. J., Macchetto, F. D., and Capetti, A. (1997). The Narrow-Line Region of NGC 4151: A Turbulent Cauldron. *ApJ*, 487:L121+.